Available online at www.sciencedirect.com
ScienceDirect
International Journal of Heat and Mass Transfer 51 (2008) 683–695
International Journal of HEAT and MASS TRANSFER
www.elsevier.com/locate/ijhmt

Large-eddy simulation of a dispersed particle-laden turbulent round jet

Thomas G. Almeida *, Farhad A. Jaberi

Department of Mechanical Engineering, Michigan State University, East Lansing, Michigan 48824-1226, USA

Received 13 October 2006; received in revised form 24 April 2007
Available online 28 June 2007

Abstract

The numerical results obtained by large-eddy simulation (LES) of a particle-laden axisymmetric turbulent jet are compared with the available experimental data. The results indicate that with a new stochastic subgrid-scale (SGS) closure, the effects of the particles on the carrier gas and those of the carrier gas on the particles are correctly captured by the LES. Additional numerical experiments are conducted and used to investigate the effects of particle size, mass-loading ratio, and other flow/particle parameters on the statistics of both the carrier gas phase and the particle dispersed phase.

Keywords: Particle-laden jet; Dilute, two-phase flows; Turbulent jet; LES

1. Introduction

Among various predictive methods available for particle-laden or droplet-laden dispersed multiphase turbulent flows, the numerical methods based on large eddy simulation (LES) are very attractive as they provide the most optimum means of capturing the unsteady physical features in these flows [1–6]. The accuracy and the reliability of LES predictions is, however, dependent on several factors such as the accurate modeling of the subgrid-scale (SGS) phase interactions and the correct representation of the initial/boundary conditions for all phases. To ensure the accuracy of a given model, both verification and validation studies should be conducted as suggested by Boivin et al. [7]. Of high importance to the development and verification of LES SGS models are both *a priori* analysis of direct numerical simulation (DNS) data, and *a posteriori* analysis of LES results via comparison with the laboratory experiments.

Armenio et al. [8] investigated the effects of the SGS on particle motion. Their work indicates that using a filtered velocity field alone to advance the particles can lead to serious inaccuracies; thus the importance of the SGS closures is emphasized. Miller and Bellan [9] conducted a thorough *a priori* analysis of the SGS effects using DNS results for a transitional mixing layer, and they also concluded that neglecting the SGS velocity fluctuations in LES might lead to gross errors in the prediction of the particle drag force. This, in turn, will lead to errors in both the carrier-phase and the dispersed-phase. Miller [10] went on to investigate the effects of solid particles on an exothermic reacting mixing layer. He found that the preferential concentration of the particles in the high-strain braid regions of the mixing layer, can lead to local flame extinction. Several other researchers have also used DNS data for a better understanding of isothermal and non-isothermal reacting and nonreacting particle-laden turbulent flows. For example, Mashayek [11,12] and Mashayek and Jaberi [13] noted that the presence of particles effectively decreases the turbulent kinetic energy while increasing the anisotropy of homogeneous turbulent shear flows. These effects were shown to be magnified by increasing either the mass-loading ratio or the particle time constant. They also found that the autocorrelation coefficient of the velocity of the carrier

* Corresponding author. Present address: General Dynamics-AIS, 1200 Joe Hall Drive, Ypsilanti, MI 48197, USA. Tel.: +1 734 480 5021; fax: +1 734 480 5367.
E-mail address: thomas.almeida@gd-ais.com (T.G. Almeida).

0017-9310/$ - see front matter © 2007 Elsevier Ltd. All rights reserved.
doi:10.1016/j.ijheatmasstransfer.2007.04.023

Nomenclature

B_M	mass transfer number
c_p	specific heat at constant pressure of fluid
D	jet diameter
d_p	particle diameter
E	total energy
f_1	coefficient related to particle velocity
f_2	coefficient related to particle temperature
f_3	coefficient related to particle temperature
J_i^α	mass flux of species α in ith direction
K	thermal conductivity
m_p	mass of particle
N_s	number of species
P	pressure
q_i	heat transfer in ith direction
R^0	universal gas constant
R	molecular weight gas constant
r	radial position
r_0	jet radius
S_E	energy source term
S_{ui}	momentum source term in ith direction
S_ρ	mass source term
T	fluid temperature
T_p	particle temperature
t	time
u_i	ith component of fluid velocity vector, **U**
u_{cl}	centerline axial velocity
u_m	mean axial velocity
u_{rms}	root-mean-square of axial velocity
$\overline{u'v'}$	Reynolds stress
u^*	fluid velocity at particle position
u_p	particle velocity
v_i	ith component of particle velocity vector, **V**
W_α	molecular weight of species α
X_i	ith component of Lagrangian coordinate system
x_i	ith component of Eulerian coordinate system
x_p	particle location
Y_α	mass fraction of species α
α_2	ratio of specific heat of the particle to that of the fluid
γ	ratio of specific heats of the fluid
η	coefficient related to particle energy
μ	fluid viscosity
ρ	fluid density
ρ_p	particle density
τ_{ij}	Newtonian fluid stress tensor
τ_p	particle time constant/Stokes number

gas in an isotropic two-phase flow increases with an increase in mass-loading ratio. Jaberi [14] and Jaberi and Mashayek [15] studied particle temperature in homogeneous turbulence. They found that the temperature intensity decreases with increasing particle time constant, thermal diffusivity and/or Prandtl number. Their results clearly indicate the importance of the thermal coupling effects and the SGS temperature interactions between phases in non-isothermal two-phase flows which should be included in the LES of such flows.

This study is intended to offer evidence that the LES and the corresponding SGS closures discussed and implemented herein are both applicable and accurate. This is accomplished through comparison with the experimental data of Gillandt et al. [16], who have generated phase-Doppler-anemometry (PDA) results for the near-field of a moderate Reynolds number round jet laden with heavy particles. Most of the reported experimental studies of particle-laden turbulent jets [17–21] consider the "far-field behavior" of the flow and/or do not measure both the carrier and dispersed phases concurrently. The goal of LES is, of course, to be able to predict the near and far flow field behavior of both phases, but it seems to be more prudent to focus first on the performance of the models in the near field. The desire to improve the applicability of LES to multiphase flows is complemented by the current limitations of experimental methods of flow measurement. For example, the PDA system [16,22] can measure the velocities of both the carrier gas and the particles, but the particles must be much larger than the tracers (to offer a definitive separation of scales). This results in a description of a flow which involves particles larger than those that may be observed in some industrial applications. In contrast, the LES methods described herein may be readily used for various particle sizes and Reynolds numbers. This work is somewhat similar to the investigation of a slit-jet by Yuu et al. [23]. However, there are important physical differences between planar and axisymmetric free jets and an additional emphasis is placed here on the effect of particle inlet conditions and SGS models.

The remainder of this paper is organized as follows: first, a description of the governing equations and computational methodology for both the carrier gas and particulate field is presented in Section 2. That is followed by a detailed discussion of the LES results, including the experimental validation in Section 3. Finally, the paper is completed by a summary and some concluding remarks in Section 4.

2. Formulation and computational methodology

In the hybrid Eulerian–Lagrangian two-phase large eddy simulation (LES) method, the "resolved" carrier gas field is obtained by solving the filtered form of the (compressible) Navier–Stokes, energy and scalar equations, together with the equation of state for pressure

$$\frac{\partial\langle\rho\rangle}{\partial t}+\frac{\partial\langle\rho\rangle_l\langle u_i\rangle_L}{\partial x_i}=\langle S_\rho\rangle_l \tag{1}$$

$$\frac{\partial\langle\rho\rangle_l\langle u_i\rangle_L}{\partial t}+\frac{\partial\langle\rho\rangle_l\langle u_i\rangle_L\langle u_j\rangle_L}{\partial x_j}=-\frac{\partial\langle p\rangle_l}{\partial x_i}+\frac{\partial\langle\tau_{ij}\rangle_l}{\partial x_j}-\frac{\partial\langle\Gamma_{ij}\rangle_l}{\partial x_j}+\langle\rho\rangle_l g_i+\langle S_{ui}\rangle_l \tag{2}$$

$$\frac{\partial\langle\rho\rangle_l\langle E\rangle_L}{\partial t}+\frac{\partial\langle\rho\rangle_l\langle u_i\rangle_L\langle E\rangle_L}{\partial x_i}=-\frac{\partial\langle q_i\rangle_l}{\partial x_i}-\frac{\partial N_i}{\partial x_i}+\langle\rho S_e\rangle_l \tag{3}$$

$$\frac{\partial\langle\rho\rangle_l\langle Y_\alpha\rangle_L}{\partial t}+\frac{\partial\langle\rho\rangle_l\langle u_i\rangle_L\langle Y_\alpha\rangle_L}{\partial x_i}=-\frac{\partial\langle J_i^\alpha\rangle_l}{\partial x_i}-\frac{\partial M_i^\alpha}{\partial x_i}+\langle\rho S_\alpha\rangle_l+\left\langle S_\rho^\alpha\right\rangle_l,\quad \alpha=1,2,\ldots,N_s \tag{4}$$

$$\langle p\rangle_l\approx\langle\rho\rangle_l R^0\langle T\rangle_l\sum_1^{N_s}\frac{\langle Y_\alpha\rangle_L}{W_\alpha} \tag{5}$$

$$\langle\tau_{ij}\rangle\approx\langle\mu\rangle_L\left(\frac{\partial\langle u_i\rangle_L}{\partial x_j}+\frac{\partial\langle u_j\rangle_L}{\partial x_i}-\frac{2}{3}\delta_{ij}\frac{\partial\langle u_k\rangle_L}{\partial x_k}\right),\quad \langle\mu\rangle_L=Pr\langle k/C_p\rangle_L, \tag{6}$$

where $\langle f(x,t)\rangle_l$ and $\langle f(x,t)\rangle_L=\langle\rho f\rangle_l/\langle\rho\rangle_l$ represent the filtered and the Favre-filtered values of the transport variable $f(x,t)$ and ρ, u_i, p, T, E, and Y_α are the fluid density, velocity, pressure, temperature, energy and mass fraction of species α, respectively. In Eq. (5), μ, k, C_p and Pr are the viscosity coefficient, the thermal conductivity coefficient, the specific heat and the Prandtl number, respectively. Also, R^0 denotes the universal gas constant and W_α is the molecular weight of species α. The SGS closures that appear in the above filtered equations include the SGS stress $\langle\Gamma_{ij}\rangle=\langle\rho\rangle_L[\langle u_iu_j\rangle_L-\langle u_i\rangle_L\langle u_j\rangle_L]$ and the SGS energy and scalar fluxes. These are modeled by standard similarity and diffusivity type closures [24–29]. The effects of particles (or evaporating droplets) on the carrier fluid are expressed through the mass (S_ρ), momentum (S_{ui}) and energy (S_e) source/sink terms as described below.

The particle field is solved via a Lagrangian method under the point-source approximation. In this method, the evolution of the particle displacement vector (X_i), the particle velocity vector (v_i), the particle temperature (T_p), and in case of evaporating particles or droplets, the particle mass (m_p), is governed by the following equations:

$$\frac{dX_i}{dt}=v_i \tag{7}$$

$$\frac{dv_i}{dt}=\frac{f_1}{\tau_p}\left(u_i^*-v_i\right) \tag{8}$$

$$\frac{dT_p}{dt}=\frac{\eta f_2}{\tau_p}(T^*-T_P)+\frac{L_v}{m_pc_L}\frac{dm_p}{dt} \tag{9}$$

$$\frac{dm_p}{dt}=-\frac{m_pf_3}{\tau_p}\ln(1+B_M), \tag{10}$$

where the asterisk refers to the local fluid variables which are interpolated to the particle position and τ_p is the normalized particle time constant. The variables η, f_1, f_2 and f_3 are functions of the particle and carrier gas parameters such as the particle drag coefficient, the particle Reynolds number, and the Prandtl number. B_M is the mass transfer number for evaporating droplets as calculated by the Langmuir–Knudsen non-equilibrium model. Note that gravity is also ignored in Eq. (8), as the relative velocities of the two phases are far greater than the terminal velocity of the particles. In the following terms:

$$\eta=\frac{\beta}{e^\beta-1},\quad \beta=-\left(\frac{3Pr\tau_p}{2}\right)\frac{1}{m_p}\frac{dm_p}{dt} \tag{11}$$

$$f_1=\frac{C_DRe_p}{24} \tag{12}$$

$$f_2=\frac{Nu}{3Pr\alpha},\quad \alpha=\frac{C_l}{C_p} \tag{13}$$

$$f_3=\frac{Sh}{3Sc} \tag{14}$$

Re_p is the Reynolds number based on the particle diameter and the slip velocity, Re_b is the blowing Reynolds number due to evaporative blowing velocity, Nu is the Nusselt number, Sh is the Sherwood number and Sc is the Schmidt number. The (non-dimensional) particle time constant is defined as $\tau_p=\frac{\rho_p d_p^2}{18\mu}$, and the drag coefficient C_D is calculated by a correlation involving Re_p.

The volumetric source terms appearing in the carrier gas equations are evaluated based on the volumetric averaging of the Lagrangian field as

$$S_\rho=-\frac{1}{\delta V}\sum\left\{-m_p\left[\frac{f_3}{\tau_p}\ln(1+B_M)\right]\right\} \tag{15}$$

$$S_{ui}=-\frac{1}{\delta V}\sum\left\{m_p\frac{f_1}{\tau_p}(u_i^*-v_i)+\frac{m_pv_{dri}}{\tau_p}-m_p\left[\frac{f_3}{\tau_p}\ln(1+B_M)v_i\right]\right\} \tag{16}$$

$$S_e=-\frac{1}{\delta V}\sum\left\{\frac{C_p\alpha}{(\gamma-1)Ma^2}m_p\left[\frac{\eta f_2}{\tau_p}(T^*-T_p)+\frac{f_1}{\tau_p}(u_i^*-v_i)v_i+\frac{v_{dri}v_i}{\tau_p}\right]-m_p\left[\frac{f_3}{\tau_p}\ln(1+B_M)\right]\left[\frac{h_{v,s}}{(\gamma-1)Ma^2}+\frac{v_iv_i}{2}\right]\right\}, \tag{17}$$

where the summation is taken over all particles in the volume $\delta V=\delta x^3$ centered at each Eulerian (grid) point.

Eqs. (1)–(17) describe the general Eulerian-Lagrangian formulation of a multi-component compressible two-phase turbulent reacting system with full mass, momentum and energy coupling between carrier and dispersed phases. For systematic assesment of the LES methodology, the SGS models, and the numerical scheme, we only consider non-evaporating particles in a dilute non-reacting two-phase system in this study. Hence, $\dot{m}_p$ and S_ρ are zero

and there is no need to solve scalar and particle mass equations. Leaving out the effects of gravity also leads to v_{dri} being zero. The other carrier-gas equations are solved together with diffusivity-type closures for the SGS stress and the SGS energy flux terms. For the particle velocity, a stochastic model is considered in which the residual or subgrid velocity of the carrier fluid at the particle location is evaluated from the SGS viscosity. The model is described below. The combined large- and small-scale fluid velocity is then used to move the particles and to calculate the particle drag force. The discretization procedure of the carrier fluid is based on the "compact parameter" finite difference scheme, which yields up to sixth order spatial accuracies. The time differencing is based on a second order method. Once the fluid velocity, density and temperature fields are known, the particle transport equations are integrated via "standard" differencing schemes. The evaluation of the fluid properties at the particle locations is based upon first and fourth order accurate Lagrangian interpolation schemes. The velocity and size of particles at the jet inlet vary in different simulations. For the simulations in this study, the Eulerian grid has 1.5 million points, while there are at least 35 thousands Lagrangian particles. The statistical properties (e.g., mean and rms velocities) are calculated over three pass-over times after the flow is fully developed.

As noted in Eq. (2), the momentum coupling between the dispersed particle phase and the carrier gas phase is through the velocity difference between phases, and the drag associated with that difference. This 'slip' velocity could be computed by interpolation of the fluid velocity to the particle location at each time step in DNS, where the fluid velocity is known at sufficiently small grid points. However, in LES, only the filtered fluid velocity field, $\langle u_i\rangle_L$, is known. Thus, it becomes necessary to model the SGS part of the fluid velocity at the particle location. The simplest estimation is to interpolate the filtered velocity only, neglecting the SGS effects of the carrier gas on the dispersed phase. This would not be a good assumption when the energy removed by filtering is large or the particle time constant is small. Another approach that is used herein is to represent the effects of SGS carrier fluid velocity on particles via a stochastic closure. In this closure, the SGS particle dispersion and the fluid Lagrangian velocity follow a history-independent diffusion process. Diffusion processes have been widely used in PDF modeling of single-phase turbulent flows [30–33].

Giscquel et al. [33] recently proposed a system of stochastic differential equations (SDEs) to solve the statistically equivalent Fokker-Plank equation of the so-called SGS velocity filtered density function via a multivariable stochastic diffusion process. A similar SDE system is used here for modeling of SGS fluid turbulence on particle dispersion. For this the particle location, the particle velocity and the total (resolved plus residual) fluid particle velocity as represented by $\mathbf{X}\equiv X_i$ and are obtained by solving the following modeled equations:

$$
\begin{aligned}
&\mathrm{d}X_i = A_i(\mathbf{X})\,\mathrm{d}t + B_{ij}(\mathbf{X})\,\mathrm{d}W_j,\\
&\mathbf{X} = \begin{bmatrix} x_{\mathrm{p}} \\ u_{\mathrm{p}} \\ u^* \end{bmatrix},\\
&\mathbf{A} = \begin{bmatrix} u_{\mathrm{p}} \\ \frac{f_1}{\tau_{\mathrm{p}}}\left(u^* - u_{\mathrm{p}}\right) \\ -\nabla\langle P\rangle + \frac{1}{Re_0}\nabla^2\langle u\rangle_L + G(u^* - \langle u\rangle_L) \end{bmatrix},\\
&\mathbf{R} = \begin{bmatrix} 0 \\ 0 \\ \sqrt{C_0\varepsilon}\,\xi \end{bmatrix},
\end{aligned}
\tag{18}
$$

where A_i and B_{ij} are respectively the drift and diffusion coefficients and W_i is a Wiener process. $\mathbf{R}$ is a vector based on the diagonal elements of the matrix B_{ij}, and ξ is the normal Gaussian random variable. Here, only one component of the velocity is shown for simplicity.

One of the SDEs in this system models the evolution of the fluid particle velocity as [33]

$$
\begin{aligned}
&\mathrm{d}u^* = \left[-\frac{\partial P}{\partial x_i} + \frac{1}{Re_0}\frac{\partial^2\langle u_i\rangle_L}{\partial x_j\partial x_j} + G_{ij}\left(u_i^* - \langle u_i\rangle_L\right)\right]\mathrm{d}t + \sqrt{C_0\varepsilon}\,dW_i,\\
&G_{ij} = -\omega\left(\frac{1}{2} + \frac{3}{4}C_0\right)\delta_{ij},
\end{aligned}
\tag{19}
$$

where $\omega = \varepsilon/k$ with $\varepsilon = C_\varepsilon k^{2/3}/\Delta_f$, $k = \tau_{ii}/2$ and C_0 is a constant. Eq. (19) is used for reconstructing the total (filtered plus SGS) fluid velocity at the particle location. It is to be noted here that the 'seen' fluid particle velocity and the fluid particle may behave differently because of the cross-trajectories effect of the gravity or the large inertia effect of large discrete phase particles. These effects are ignored in this study. Eq. (18) is solved with the Euler–Maruyama numerical scheme:

$$
\mathbf{X}^{n+1} = \mathbf{X}^n + \mathbf{A}^n\Delta t + \mathbf{R}^n\sqrt{\Delta t}. \tag{20}
$$

3. Results and discussion

3.1. Comparison with experiment

An *a posteriori* analysis is conducted to assess the stochastic particle closure and the overall performance of LES for computing two-phase turbulent flows. Specifically, LES and experimental results for a particle-laden axisymmetric turbulent jet are compared. The experimental results are taken from Gillandt, et.al. [16], in which a phase-Doppler anemometry (PDA) system is used to measure the velocities of the seeded carrier gas and heavy glass particles. The physical parameters for the two-phase flow configuration are given in Table 1. The results for the single-phase flow configuration are also included, although an emphasis is placed on the ability of LES to accurately represent multiphase effects. In the numerical simulations, the inlet mean velocity profiles in the axial-direction of both phases are taken from the experimental results 1 mm downstream of

Table 1
Physical parameters in experiment

Reynolds number	5700
Nozzle diameter	12 mm
Carrier gas	Air
Mean particle diameter	110 μm
Mass loading	1
Dispersed phase	Glass beads

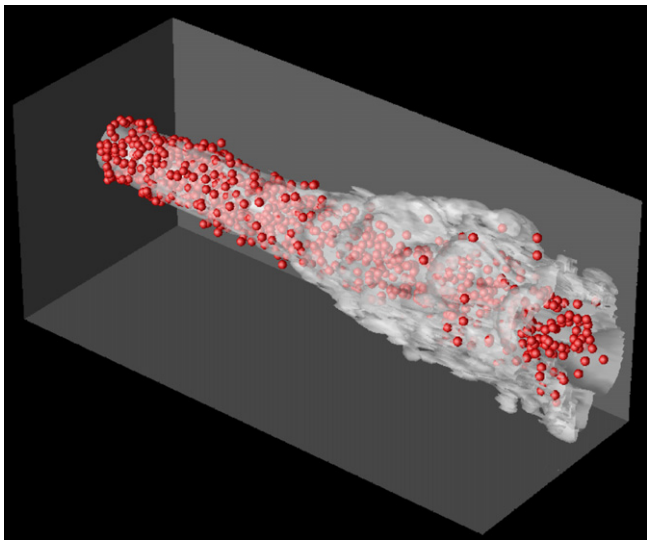

Fig. 1. Vorticity magnitude and particle distribution in a typical two-phase gas-particle turbulent jet simulation. Small numbers of particles are shown and the particle size is exaggerated for sake of clarity.

Table 2
Particle conditions in various cases

Case	SGS particle model	Particle size distribution
1	No	Uniform
2	Yes	Uniform
3	Yes	Gaussian

the nozzle and interpolated onto the computational grid; the inlet velocity of the carrier phase in the radial direction is forced harmonically, while that of the particles is unforced. Fig. 1 shows vorticity magnitude and particles in one of our simulations.

The data for three different LES cases are compared to the experimental results. The parameters of all three cases are given in Table 2. In case 1, no SGS model is used for particle-carrier gas interactions and particles are injected with uniform size at jet inlet. In case 2, the stochastic SGS model described in Section 3 is used for the SGS particle dispersion but still the particles have a uniform size distribution at inlet. Finally, in case 3, the stochastic SGS model is used with a clipped-Gaussian particle size distribution at jet inlet. The results are reported for both single- and two-phase flows.

Fig. 2 shows a comparison between experimental and computational values of centerline mean axial velocity,

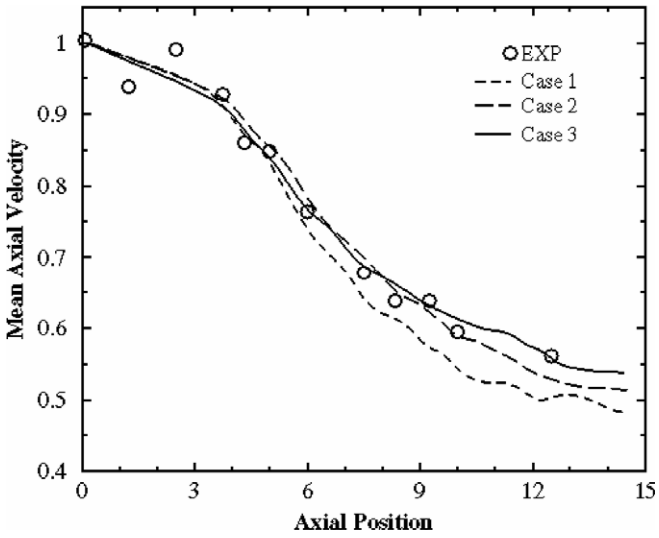

Fig. 2. Centerline mean axial velocity versus downstream location. "EXP" stands for the experiment.

u_m, at various downstream locations. Case 3, the case with SGS particle closure and initial non-uniform (Gaussian) particle size distribution, best reproduces the experimental results. Case 2 is nearly as accurate as case 3 and case 1 is considerably less accurate in comparison to the other cases. This indicates that the SGS closures are indeed viable. Also, the slightly better results for case 3 as compared to those for case 2 suggest that some of the differences between experimental and LES results are due to inconsistencies in the inlet particle conditions (i.e. particle size and locations) and are not due to modeling. The difference between experimental and numerical results is better shown in Table 3, where the "percentage of error" in the predicted values of the centerline axial velocity at several axial locations is listed. The results in Table 3 confirm that the predicted centerline velocity in case 3 is the closest to the experiment at all locations from the nozzle.

Fig. 3 shows the radial variations of mean axial velocity at two different axial locations and Table 4 gives the corresponding error values for those locations. Overall, there is a good match between experimental and numerical results. The error calculations indicate that there are positions where each simulated case best matches the experimental data. However, on average, the results of case 3 are noticeably better than the other two. Other flow statistics are also well predicted by LES, provided that appropriate SGS

Table 3
Percentage of the difference between experimental and LES values of mean axial velocity at jet centerline, at several axial locations

Axial location (x/D)	LES Case 1	LES Case 2	LES Case 3
1.25	4.24	3.70	3.69
6	3.93	1.63	0.09
7.5	5.49	3.96	1.40
9.25	10.46	2.34	1.35
12.5	10.40	2.29	0.27

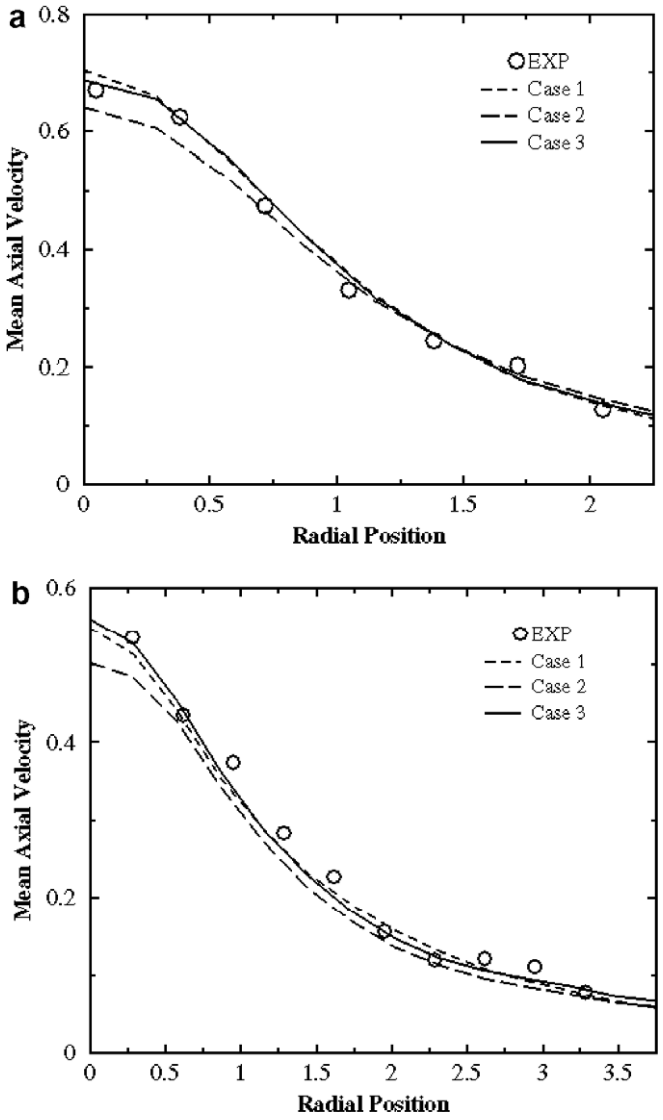

Fig. 3. Axial velocity profiles: (a) $x/D = 7.5$; (b) $x/D = 12.5$.

Table 4
Percentage of the difference between experimental and LES values of mean axial velocity at some radial and axial locations

Axial location (x/D)	Radial location (r/r_0)	LES Case 1	LES Case 2	LES Case 3
2.5	0.3	0.42	0.42	0.45
5	1.2	12.31	9.72	11.64
12.5	0.3	9.75	4.16	1.52
12.5	2.3	5.92	9.15	1.56

model and boundary conditions are employed. This is shown in Fig. 4a, where the radial profiles of the root-mean-square (rms) values of axial velocity, u_{rms} as measured experimentally and compared with the LES results of case 3 are shown. The corresponding percent error values are presented in Table 5. Again, it is observed that the LES predictions are in good overall agreement with the experimental results, despite some differences at locations far from nozzle and jet centerline. It is important to note that the magnitude of the turbulence intensity is relatively small and more sensitive to inlet flow/particle conditions which are not exactly the same in experiment and LES. It is also important to note that the experimental results represent one cross-sectional slice of the jet, while the LES results represent an azimuthally averaged radial profile. Considering the precision of the centerline quantities (where there is no significant difference in sampling), it is not unreasonable to assume that some of the errors observed in the radial profiles may be due to differences in sampling method. Some of the errors may also be attributed to the finite size effect of particles (e.g., particle wake) on the carrier fluid. Additionally, in the simulations considered in this paper, the inlet radial location of all (small and large) particles is randomly selected and there is effectively no particle size distribution in the radial direction at jet inlet which may not be consistent with the experiment.

To further validate the accuracy of the SGS models, comparisons between experimental and LES data are made for the case of single-phase flow. This enables the verification of the effects of the particles on the carrier gas. As shown in Fig. 4b and c, there are good agreements between the experiment and the LES in both single- and two-phase flow configurations, a clear indication that the SGS models employed are viable. The results of both the experiment and the LES show that adding heavy particles to the flow causes the centerline velocity to decay at a slower rate. This can be rationalized in that the heavy particles effectively pull the carrier gas along with their rate, slowing the deceleration due to their inertia effects. An increase in turbulence intensity is also noted when particles are added to the flow, which is also consistent with the experiment.

3.2. Flow-particle interactions

In Section 3.1, we have partially validated our LES models and numerical scheme by comparing the numerical results with the experimental data. In this section, we go beyond experiment and further examine the interactions between the carrier gas phase and the particle phase in a turbulent jet via our LES model. For instance, Fig. 5 shows the effect of average particle inertia or particle mass on the particle velocity field. It is to be noted that the experiment was conducted with relatively heavy particles, with $\tau_p = 57.4$. The heavy particles tend to follow their own path rather than the path of a fluid particle (although they still decelerate and grossly affect the carrier gas). Experimentally, it is difficult to consider smaller particles due to the interference of the particle phase with the seeded (fluid tracking) particles. It is not however very difficult to perform numerical simulations with smaller average τ_p. In all the cases shown in Fig. 5, the inlet particle size/mass is randomly selected from a clipped-Gaussian distribution about a mean particle mass or time constant, and there is no correlation between particle mass and location and/or velocity at jet inlet. Furthermore, the particles are given a

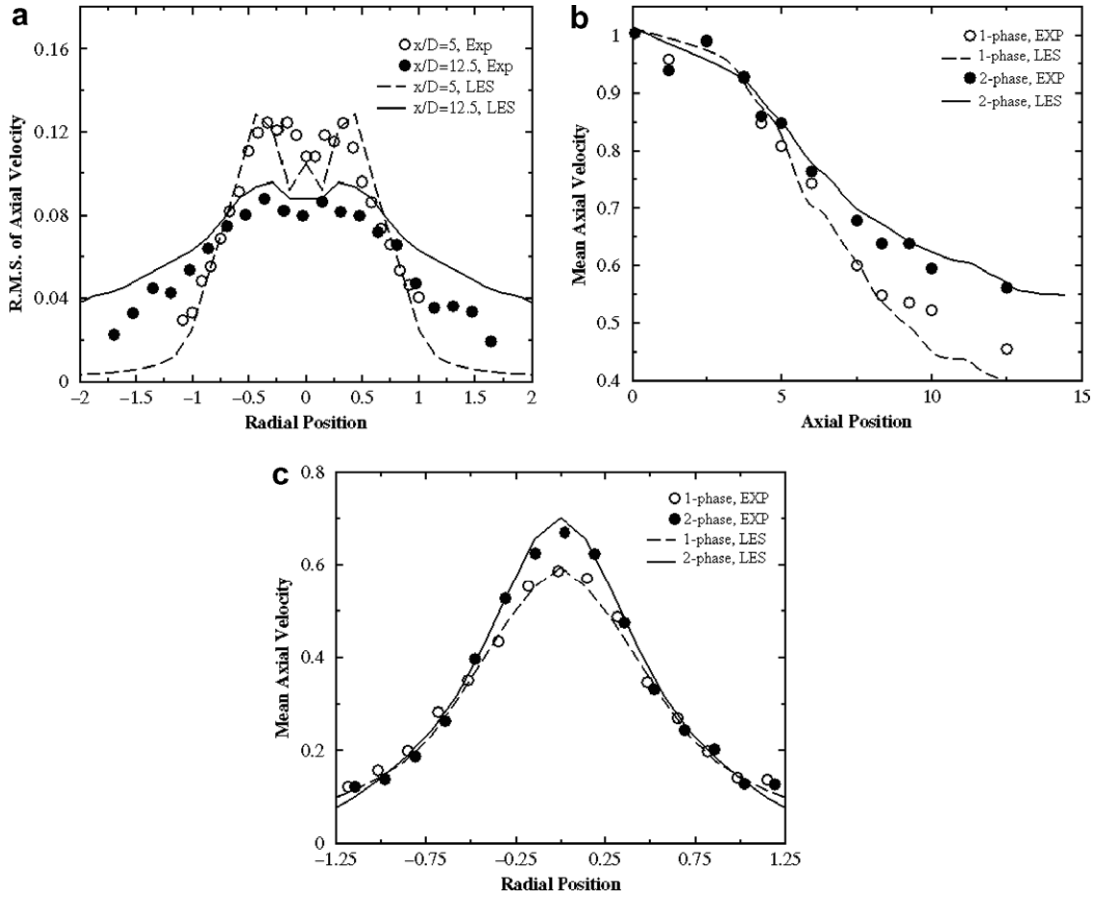

Fig. 4. (a) Radial profiles of rms of axial velocity at $x/D = 5$ and 12.5; (b) mean centerline axial velocity of single- and two-phase flow; (c) radial profiles of mean axial velocity at $x/D = 7.5$.

Table 5
Sample percent error calculations for u_{rms}

Axial location (x/D)	Radial location (r/r_0)	Case 1	Case 3
5	0.4	32.8	7.38
5	0	93.7	3.12
12.5	0.9	35.9	7.71
12.5	0.1	22.9	2.05

velocity that is nearly uniform and close to the local carrier gas velocity. As expected, Fig. 5 shows that the larger particles tend to keep their initial velocity and the smaller ones deviate more from their initial velocity due to drag force. However, a comparison between Fig. 5a and b for different mean particle inertia indicates that for particles with smaller mean time constants or inertia the correlation between particle mass and velocity is small and does not change significantly in the axial direction. For particles with larger mean inertia, a correlation between the particle mass and velocity is shown to develop as the jet evolves. This suggests that the particle velocity is much more dependent on the particle inertia when the mean particle time response is sufficiently larger than the flow time scales. For particles with bigger mean size or mass, the velocity of the carrier gas decreases much more rapidly than the particles. The 'large' particles tend to keep their initial velocity but the "small" particles quickly adjust to local jet velocity. Therefore, as the jet develops the velocity of larger particles deviate more from those with smaller mass, leading to the development of a strong correlation between particle mass and velocity in Fig. 5a. For particles with smaller mean size or mass, the particle velocity distribution at any distance from the nozzle is close to that of the fluid velocity at that location as the smaller particles quickly 'catch up' with the flow and the correlation between particle mass and velocity remain small. Of course very heavy particles never respond to the flow and keep their inlet/initial velocity-mass correlation, whatever that may be.

In the simulations considered in this paper, the initial velocity of all (small and large) particles is exclusively in the axial direction. As expected, some of the smaller particles gain a radial velocity component from the carrier gas two-way interactions and deviate from their original radial location as they move downstream (Fig. 6a). However, the larger particles tend to remain in the core of the flow. Once again, a comparison between Fig. 6a and b shows that the initial mean particle size has a significant effect on the downstream trends in the particle size/velocity distribution. Because the particles in Fig. 6b are all small, they tend to spread out of the jet core more readily.

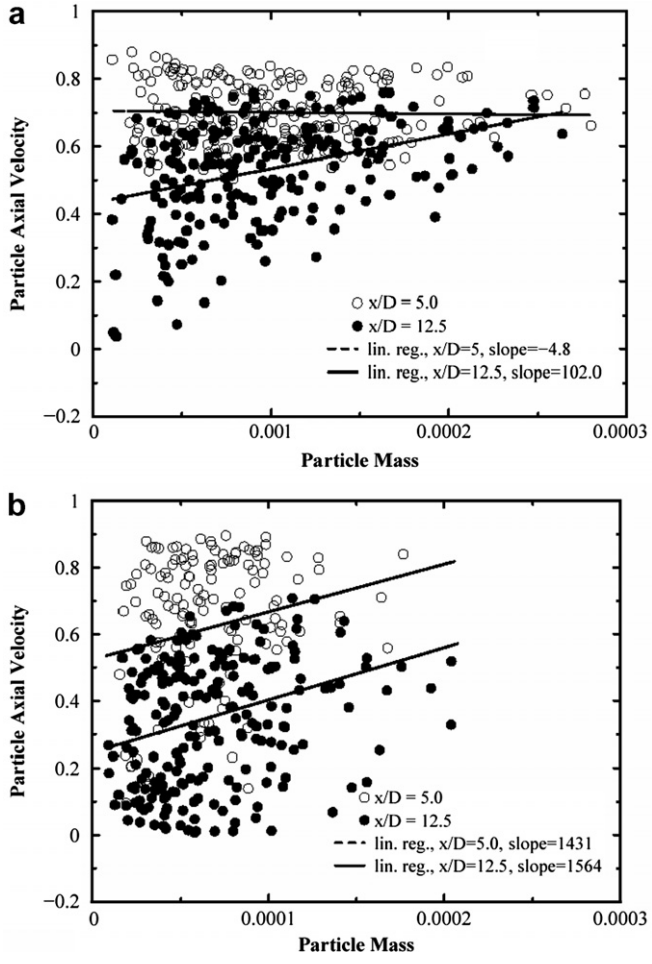

Fig. 5. Correlation between particle axial velocity and particle mass at different downstream locations: (a) $\tau_p = 57.4$; (b) $\tau_p = 10.0$. The linear regression is intended to show a general trend, not an empirical relationship.

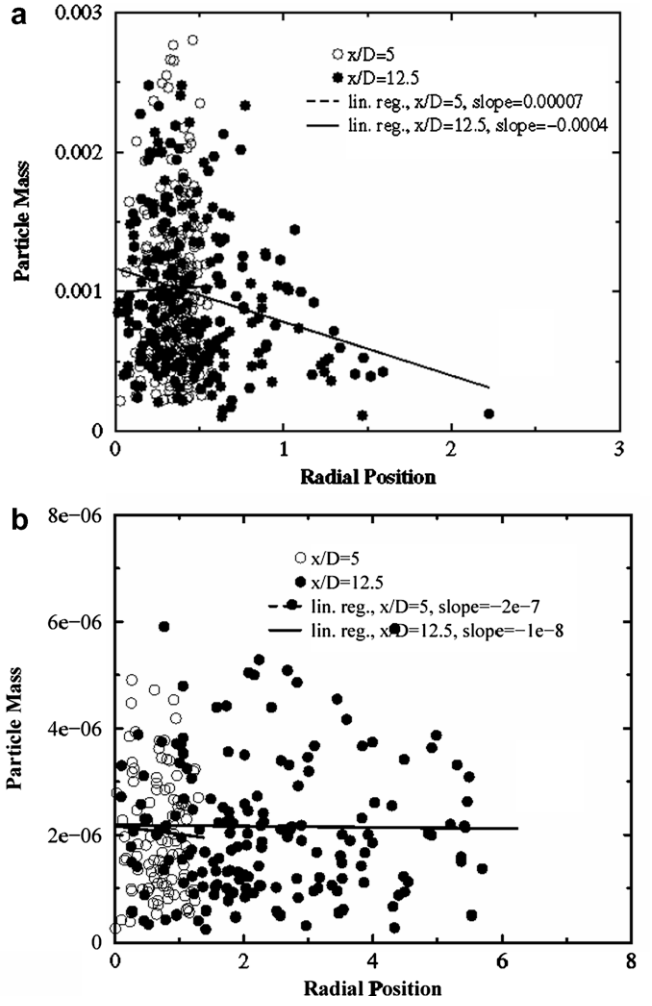

Fig. 6. Particle mass versus radial position at different downstream locations: (a) $\tau_p = 57.4$ and (b) $\tau_p = 10.0$. The linear regression is intended to show a general trend, not an empirical relationship.

Fig. 7 shows the "preferential concentration" of particles in the jet by comparing the particle number density profile with the average particle mass profile, again for two different initial mean particle time constants. These "Eulerian" particle values are obtained by averaging the "Lagrangian" particle mass and number density. Evidently, the total number of particles entrained/remained in the core of the jet increases in the axial direction for large mean particle time constants, forcing the average particle mass to decline at centerline. This does not mean that the larger particles are being replaced by smaller ones. It seems more likely that the average mass is decreasing due to the addition of smaller particles, not the loss of large particles. This also may be due to the fact that the larger particles are swept downstream at a high velocity while some of the smaller particles are caught in low vorticity regions near the core of the jet. Both the average particle mass and particle number density plots indicate that there is noticeable particle dispersion at $x/D = 12.5$, as evidenced by the "non-zero" values of these variables beyond $r/D = 0.7$. The smaller time constant case contrasts with the larger time constant case in that the particle number density has the opposite trend with axial distance. While the particle number density at jet core increases as jet develops in case with average $\tau_p = 57.4$, it actually decreases in the case with $\tau_p = 10.0$. There is also much more particle dispersion and higher particle mass/number density beyond $r/D = 0.7$ in the $\tau_p = 10.0$ case, which is expected. In this case, there are not so many "large" particles that are essentially "stuck" in their radial location by their inertia. Instead, the particles are much more likely to follow the flow and react to the changing velocity field. The radial distribution of particle size or mass seems to obey the same trend for both the $\tau_p = 57.4$ and $\tau_p = 10.0$ cases. It is also interesting to note that there are significant declines in both the average particle mass and the particle number density near the shear layer in both cases.

The probability density function (PDF) of the particle mass is shown in Fig. 8. These PDFs are obtained by sampling the data over the entire plane perpendicular to the jet, so local particle distribution is not distinct, only general axial trends are captured. It is to be reminded that at jet

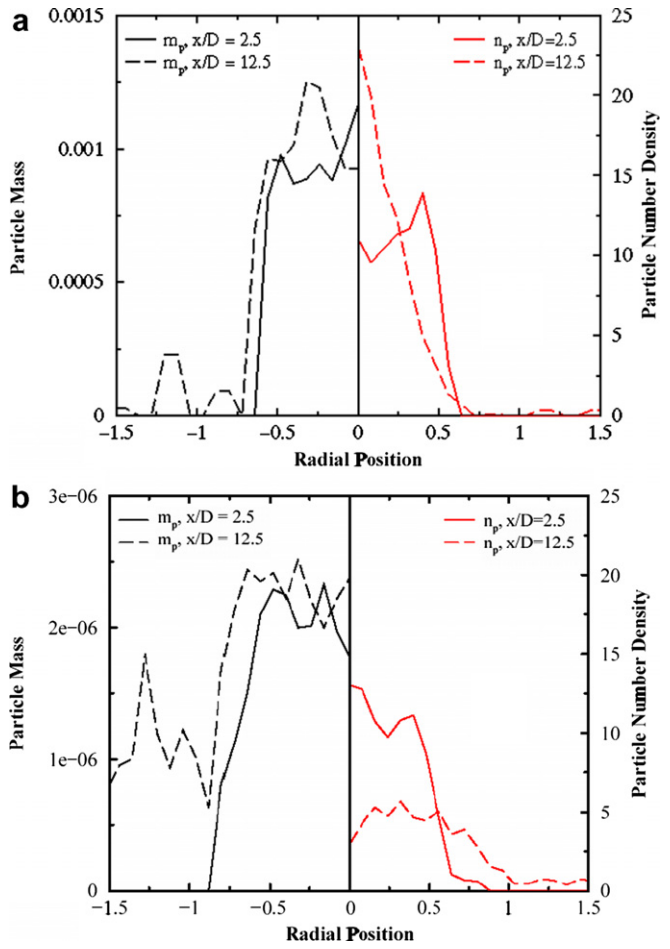

Fig. 7. Particle mass and number density, radial variation at different axial locations: (a) $\tau_p = 57.4$ and (b) $\tau_p = 10.0$.

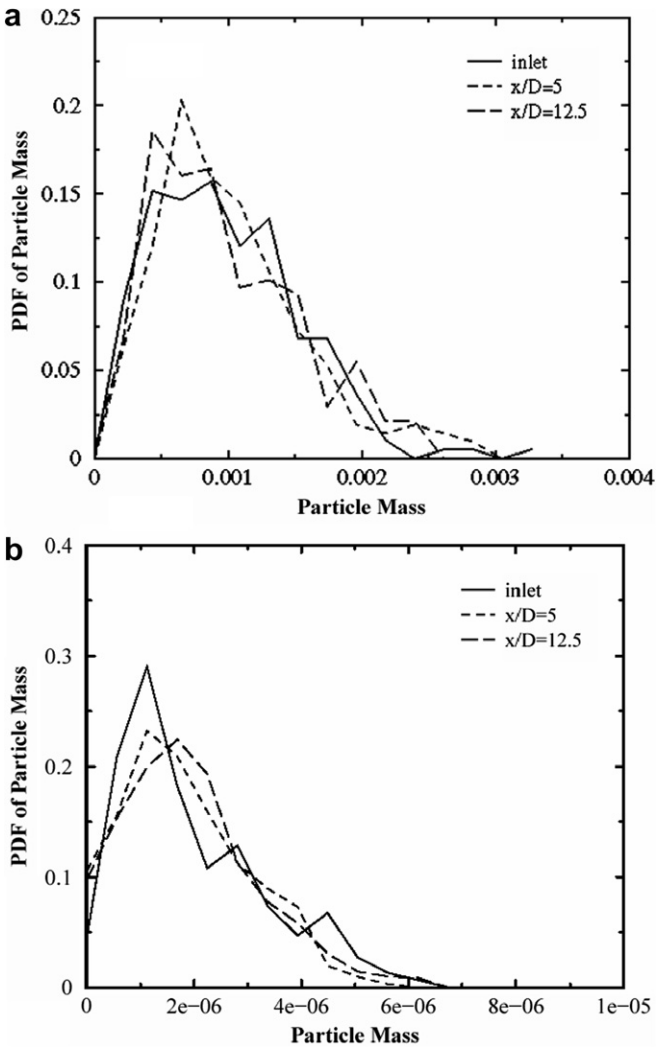

Fig. 8. Probability distribution function of particle mass: (a) $\tau_p = 57.4$ and (b) $\tau_p = 10.0$.

inlet the particle diameter is randomly selected from a clipped Gaussian distribution, resulting in a positive skewness of the particle mass PDF. The skewness indicates that there are more excursions from the mean on the larger particle mass side. This distribution remains nearly constant at different axial locations, and is nearly independent of initial mean particle size ($\tau_p = 57.4$ vs. $\tau_p = 10.0$), as shown in Fig. 8.

Fig. 9 shows the axial variations of the particle-carrier gas velocity correlations, which are obtained from the data averaged over the plane perpendicular to the jet at each axial location. The velocity correlations are calculated by the following equation (given here for $\overline{u_p u^*}$)

$$R_{u*up} = \frac{\overline{u_p u^*} - \overline{u_p} \cdot \overline{u^*}}{\sqrt{\left(\overline{u_p u_p} - \overline{u_p} \cdot \overline{u_p}\right)\left(\overline{u^* u^*} - \overline{u^*} \cdot \overline{u^*}\right)}} \tag{21}$$

The correlations between the axial velocity of the particles and the two components of the carrier gas velocity, $\overline{u_p u^*}$ and $\overline{u_p v^*}$, where the asterisk ($*$) again denotes the carrier gas property interpolated to the particle position, are the most significant for both mean particle sizes. This indicates that the ability to predict the carrier gas velocity field, knowing the particle axial velocity, is better than the ability to do so knowing the radial velocity of the particles. The velocity correlations for the larger particles decay along the axial direction as expected, indicating that there is an increased randomness in the slip velocity farther downstream as expected. This is not true for the smaller particles. For the case with smaller particles, the particle-carrier gas velocity correlations change sign downstream of the jet inlet (see Fig. 9b). Also, for the larger particle case, the radial components of the particle velocities are not very well correlated to either of the carrier gas velocities ($\overline{v_p v^*}$ and $\overline{v_p u^*} \approx 0$). It is interesting that the radial velocity of the carrier gas correlates with the axial velocity of the particles better than it does with the radial velocity of the particles when integrated over the length of the jet, as shown in Fig. 9a. One would also expect that if the particle time constant were to be decreased enough, eventually the particles would act as fluid particles and the velocity correlations would actually increase. Because of the high mass-loading ratio of these experiments and the high computational cost of solving the Lagrangian particle equations, this last case was not conducted.

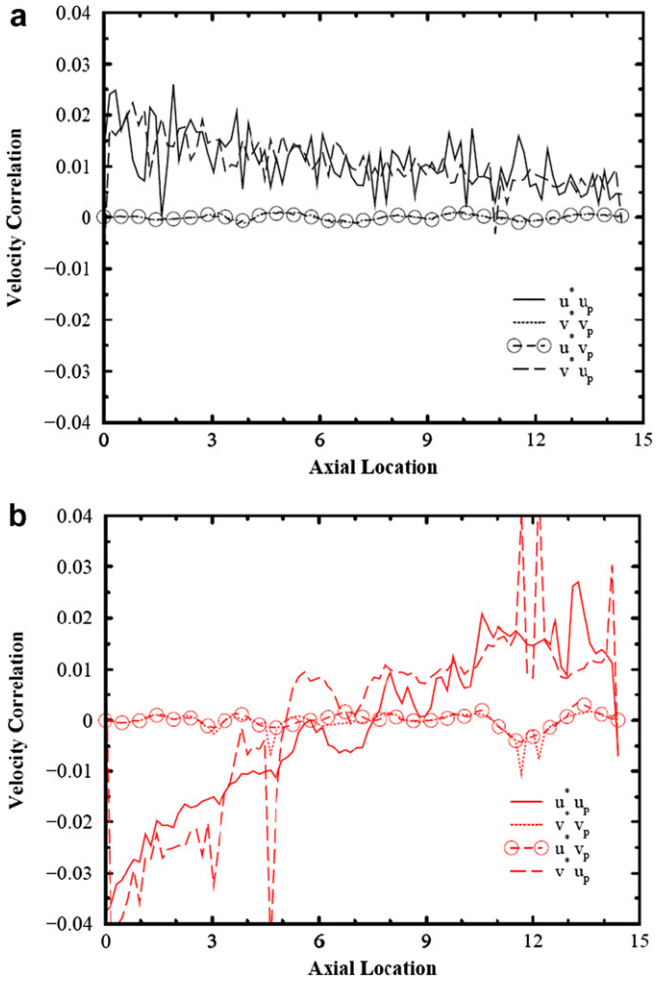

Fig. 9. Axial variation of correlation between particle and carrier gas velocities: (a) $\tau_p = 57.4$ and (b) $\tau_p = 10.0$.

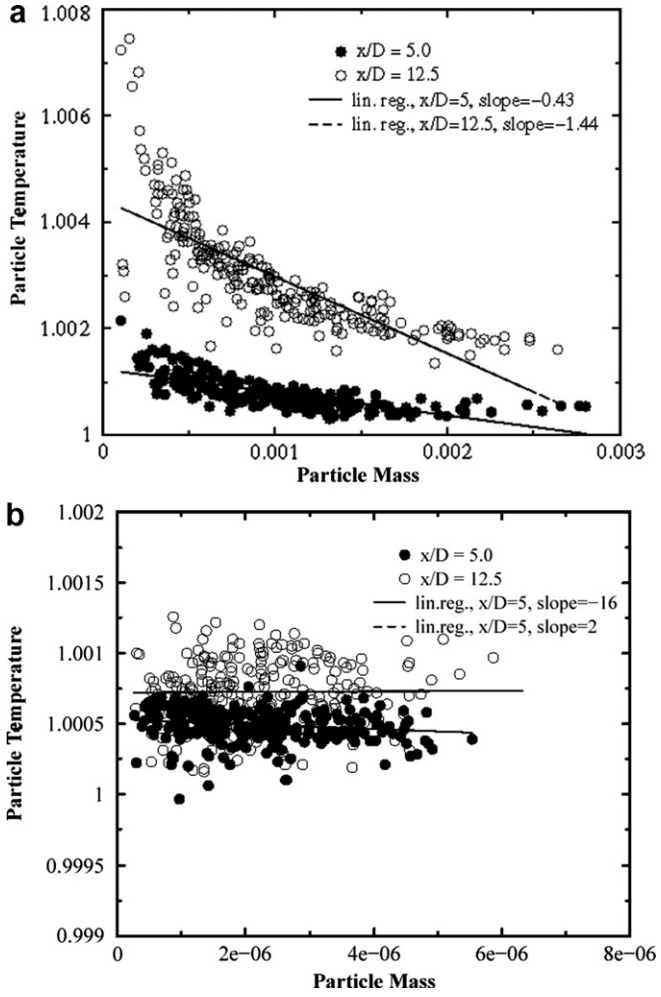

Fig. 10. Normalized particle temperature as a function of particle mass; (a) $\tau_p = 57.4$ and (b) $\tau_p = 10.0$.

One of the more difficult problems facing experimentalists is that of accurately measuring/resolving both temperature and velocity fields of highly turbulent flows. This is especially difficult for two-phase flow systems. In our simulations, the temperature variations in both phases are considered, even though these variations are not very significant due to "isothermal" flow conditions. Fig. 10 helps in better understanding of the "thermal inertia" effects of the particles on the particle and carrier gas temperature fields. As the smallest scales of the carrier gas dissipate turbulent kinetic energy into the internal energy, a significant part of that energy is transferred to the particles [13–15]. Fig. 10a shows that the temperature of the particles is, in fact, increased as the jet develops. There is also an increase in the difference between temperature of large and small particles. In the near field, all particles are at nearly the same temperature; while further downstream the smaller particles attain higher temperatures in comparison to the larger ones as the large particles do not respond very well to the carrier gas temperature fluctuations and energy dissipation. This can affect the carrier gas temperature field and, for sufficiently large temperature variations, the fluctuating velocity field. Fig. 10b shows that the particles in the case with average Stokes number of $\tau_p = 10.0$ act much less as thermal energy sinks due to their small inertia and have somewhat more uniform and lower temperature as compared to those in the case with $\tau_p = 57.4$. The results in Fig. 10 also suggest that the particles with "moderate" size/mass absorb more of the dissipated turbulent kinetic energy than the very small or very large particles. This could be due to an increase in (small scale) turbulent kinetic energy by particles, or an increase in thermal phase interactions, or both [14,15].

The results in Fig. 4 show the effects of particles on the carrier gas turbulence for relatively large particles with average $\tau_p = 57.4$, similar to that in the experiment. Figs. 11 and 12 show these effects for different average particle size and mass loading ratios. The results in Fig. 11a indicate that at $x/D = 5.0$ the turbulence is attenuated and the RMS values of the fluid axial velocity decreases by the particles regardless of particle Stokes number and mass loading ratio. As expected, the attenuation is more significant for the cases with larger average particle sizes and larger mass loading ratios. However, as shown in Fig. 11b, the

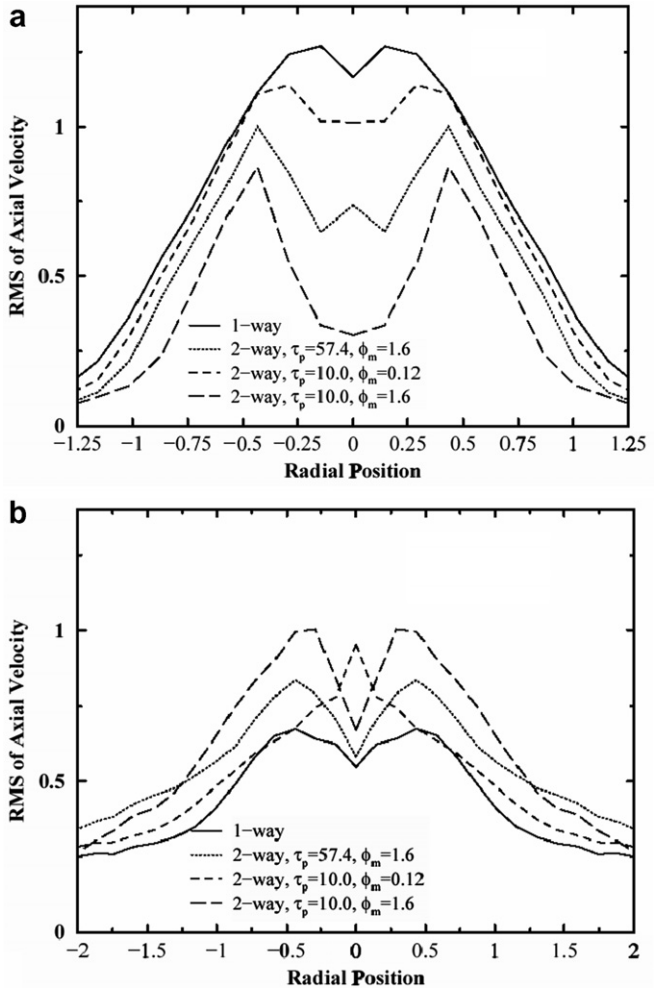

Fig. 11. RMS of axial velocity versus radial position for varying average particle inertia and mass-loading ratio: (a) $x/D = 5$ and (b) $x/D = 12.5$.

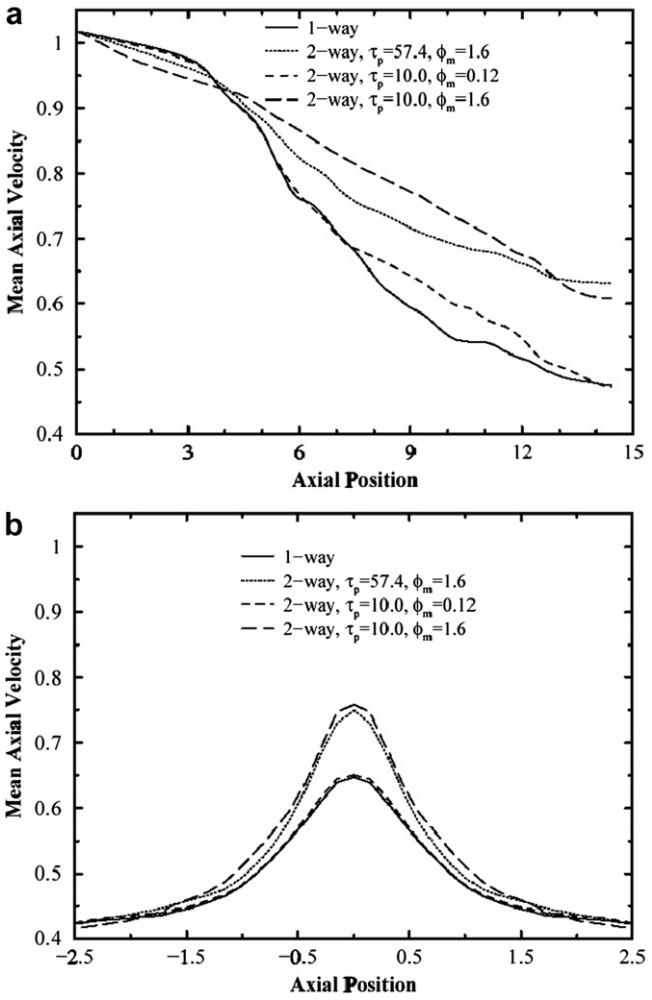

Fig. 12. Mean axial velocity: (a) versus axial position at the centerline and (b) versus radial position at $x/D = 12.5$.

effect of particles on the fluid seems to be different at downstream locations (e.g., $x/D = 12.5$), where the turbulent fluctuation of the fluid axial velocity in two-phase simulations are higher than those in single-phase flow simulations. This is due to the fact that the simulated particle-laden two-phase jet decays slower than the single-phase jet (Fig. 12). As Fig. 7 suggests, at downstream locations far enough from the jet inlet, the average particle mass or size outside the jet core is smaller than that close to centerline in both cases, even though the smaller particles in $\tau_p = 10.0$ case disperse more than the larger ones in $\tau_p = 57.4$ case. The smaller particles interact more with the turbulence, resulting in lower variance at $-1.25 > r/D$ or $r/D > 1.25$ in $\tau_p = 10.0$ case in comparison with that in $\tau_p = 57.4$ case (Fig. 11b). The larger particles are concentrated closer to centerline and consequently damp the flow more at $-1.25 < r/D < 1.25$.

Fig. 12 provides further evidence that the size of particles in two-phase jets can be very important. It shows a plot of the mean axial velocity versus axial position at the jet centerline and versus radial position at $x/D = 12.5$. Note that in Fig. 12a the effects of the particles are minimized when their size is decreased. This is due to the inlet conditions. In all three two-phase cases, the particles are initialized at a velocity that is less than that of the carrier gas. In the cases with larger particles, the particles have a large inertia, and effectively drag the carrier gas along at their velocity, while the smaller particles generally interact in a more complicated way. The smallest particles appear to have no effect on the mean flow, while the larger particles significantly decrease the decay of the centerline velocity. The plot of radial variation of axial velocity indicates that the momentum damping effects are more closely related to the mass-loading ratio than they are to the particle size, as the smaller mass-loading case nearly matches the one-way coupled case at $x/D = 12.5$, while the two larger mass-loading cases seem to match each other favorably.

4. Summary and conclusions

The abilities of large eddy simulation (LES) methods to predict multiphase turbulent flows was investigated via an *a posteriori* study, correlating experimental and numerical

results for an axisymmetric turbulent round jet laden with heavy particles. The results indicate that the subgrid-scale (SGS) carrier gas stress model and stochastic SGS model employed for particles in the LES are viable and the latter increase the accuracy of the numerical prediction by as much as 10 %. In addition to the results for two-phase flow, results were considered for the single-phase flow, for which the LES utilizing the "standard" SGS closures was found to be accurate. Various two-phase flow simulations were conducted. Of these, the simulation utilizing both the stochastic particle SGS model and the non-uniform (Gaussian) inlet particle size distribution most accurately predicted the various measured turbulent quantities, while the simulation that did not incorporate either of these two was the least precise. The simulation that included the SGS particle model, but with uniform particle size distribution at jet inlet, was reasonably accurate, but less so than the case with the Gaussian inlet particle size distribution.

Further analysis of LES data indicates a "complete" two-way coupling between velocity and temperature of particle and carrier gas phases. As the carrier gas velocity fluctuations are damped by the particles, the dissipation rate of turbulent kinetic energy decreases, and the particle temperature increases. While the velocity and temperature distribution of the small particles widens as the jet develops, those of the large particles remains nearly constant. As expected, the larger particles tend to keep their initial velocity, while the smaller particles tend to accelerate and/or decelerate more readily, and thus have a more disperse correlation between mass and velocity. Analysis of particle number density and average particle mass profiles supports these findings. However, for smaller particles, the particle number density profile widens with axial distance, indicating less entrainment of particles. The probability density functions (PDFs) of the particle mass indicate that the size density remains relatively the same in the axial direction of the flow, regardless of the initial mean particle size.

The particle-carrier gas velocity correlations for large particles show a decreasing trend in the axial direction, which is most likely due to the increase in the slip velocity between the particles and the carrier gas. For smaller particles, however, the velocity correlations actually increase in the axial direction. The dominant correlations are those between the axial velocity of the particles and the axial and radial velocities of the carrier gas; the correlations between the radial velocity of the particles and the axial and radial velocities of the carrier gas are approximately zero. Further analysis based on modifying the average particle inertia indicates that the evolution of turbulence field in two-phase jets is greatly affected by the choice of mean particle size.

Acknowledgements

This work was sponsored by the US Office of Naval Research under Grant N00014-01-1-0843. Dr. Gabriel Roy was the Program Manager for this grant. Additional support was provided by the National Science Foundation under Grant CTS0092665.

References

[1] J. Bellan, Perspectives on large eddy simulations for sprays: Issues and solutions, Atom. Sprays 10 (2000) 409–425.
[2] E. Loth, Numerical approaches for motion of dispersed particles, droplets and bubbles, Prog. Energy Comb. Sci 26 (2000) 161–223.
[3] D. Lakehal, On the modeling of multiphase turbulent flows for environmental and hydrodynamic applications, Int. J. Multiphase Flow 28 (2002) 823–863.
[4] F. Mashayek, R.V.R. Pandya, Analytical description particle/droplet-laden turbulent flows, Prog. Energy Comb. Sci. 29 (2003) 329–378.
[5] A. Elhami Amiri, S. Kazemzadeh Hannani, F. Mashayek, Large-eddy simulation of heavy-particle transport in turbulent channel flow, Num. Heat Trans., Part B: Fund. 50 (4) (2006) 285–313.
[6] S. Geiss, A. Dreizler, Z. Stojanovic, M. Chrigui, A. Sadiki, J. Janicka, Investigation of turbulence modification in a non-reactive two-phase flow, Exp. Fluids 36 (2) (2004) 344–354.
[7] M. Boivin, O. Simonin, K. Squires, On the prediction of gas-solid flows with two-way coupling using large eddy simulation, Phys. Fluids 12 (8) (2000) 2080–2090.
[8] V. Armenio, U. Piomelli, V. Fiorotto, Effect of the subgrid scales on particle motion, Phys. Fluids 11 (10) (1999) 3030–3042.
[9] R. Miller, J. Bellan, Direct numerical simulation and subgrid analysis of a transitional droplet laden mixing layer, Phys. Fluids 12 (3) (2000) 650–671.
[10] R. Miller, Effects of nonreacting solid particles and liquid droplet loading on an exothermic reacting mixing layer, Phys. Fluids 13 (2001) 3303–3320.
[11] F. Mashayek, Droplet-turbulence interactions in low-Mach-number homogeneous shear two-phase flows, J. Fluid Mech. 367 (1998) 163–203.
[12] F. Mashayek, Direct numerical simulations of evaporating droplet dispersion in forced low Mach number turbulence, Int. J. Heat Mass Transfer 41 (1998) 2601–2617.
[13] F. Mashayek, F. Jaberi, Particle dispersion in forced isotropic low-Mach-number turbulence, Int. J. Heat Mass Transfer 42 (1999) 2823–2836.
[14] F.A. Jaberi, Temperature fluctuations in particle-laden homogeneous turbulent flows, Int. J. Heat Mass Transfer 41 (1998) 4081–4093.
[15] F.A. Jaberi, F. Mashayek, Temperature decay in two-phase turbulent flows, Int. J. Heat Mass Transfer 43 (2000) 993–1005.
[16] I. Gillandt, U. Fritsching, K. Bauckhage, Measurement of phase interaction in dispersed gas/particle two-phase flow, Int. J. Multiphase Flow 27 (2001) 1313–1332.
[17] E. Longmire, J. Eaton, Structure of a particle-laden round jet, J. Fluid Mech. 236 (1992) 217–257.
[18] C.A. Kennedy, J.H. Chen, Mean flow effects on the linear stability of compressible planar jets, Phys. Fluids 10 (1998) 615.
[19] Y. Tsuji, Y. Morikawa, T. Tanaka, K. Karimine, S. Nishida, Measurement of an axisymmetric jet laden with coarse particles, Int. J. Multiphase Flow 14 (1988) 565–574.
[20] F. Prevost, J. Boree, H.J. Nuglisch, G. Charnay, Characterization of a polydispersed particle-laden jet using a phase Doppler anemometer, in: Proceeding of ICLASS, 1994, pp. 938–945.
[21] J-S. Shuen, P. Solomon, Q-F. Zhang, G.M. Faeth, Structure of particle-laden jets: Measurements and predictions, AIAA J. 23 (1985) 396–404.
[22] L. Aisa, J.A. Garcia, L.M. Cerecedo, I.G. Palacin, E. Calvo, Particle concentration and local mass flux measurements in two-phase flows with PDA. Application to a study on the dispersion of spherical particles in a turbulent air jet, Int. J. Multiphase Flow 28 (2002) 301–324.

[23] S. Yuu, T. Ueno, T. Umekage, Numerical simulation of the high Reynolds number slit nozzle gas-particle jet using subgrid-scale coupling large eddy simulation, Chem. Eng. Sci. 56 (2001) 4293–4307.
[24] F.A. Jaberi, P.J. Colucci, Large eddy simulation of heat and mass transport in turbulent flows. Part 1: Velocity field, Int. J. Heat Mass Transfer 46 (2003) 1811–1825.
[25] F.A. Jaberi, P.J. Colucci, Large eddy simulation of heat and mass transport in turbulent flows. Part 2: Scalar field, Int. J. Heat Mass Transfer 46 (2003) 1827–1840.
[26] B-C. Wang, E. Yee, J. Yin, D.J. Bergstrom, A general dynamic linear tensor-diffusivity subgrid-scale heat flux model for large-eddy simulation of turbulent thermal flows, Num. Heat Trans., Part B: Fund. 51 (3) (2007) 205–227.
[27] J. Worthy, P. Rubini, A study of les stress and flux models applied to a buoyant jet, Num. Heat Trans., Part B: Fund. 48 (3) (2005) 235–256.
[28] O. Labbé, P. Sagaut, E. Montreuil, Large-eddy simulation of heat transfer over a backward-facing step, Num. Heat Trans., Part A: Apps. 42 (1–2) (2002) 73–90.
[29] T. Cziesla, E. Tandogan, N.K. Mitra, Large-eddy simulation of heat transfer from impinging slot jets, Num. Heat Trans., Part A: Apps. 32 (1) (1997) 1–17.
[30] S.B. Pope, Turbulent Flows, Cambridge University Press, Cambridge, UK, 2000, pp. 463–557.
[31] P. Givi, Subgrid scale modeling in turbulent combustion: A review, AIAA Paper No. AIAA-03-5081, 2003.
[32] F.A. Jaberi, P.J. Colucci, S. James, P. Givi, S.B. Pope, Filtered mass density function for large-eddy simulation of turbulent reacting flows, J. Fluid Mech. 401 (1999) 85–121.
[33] L.Y.M. Giscquel, P. Givi, F.A. Jaberi, S.B. Pope, Velocity filtered density function for large-eddy simulation of turbulent flows, Phys. Fluids 14 (2002) 1196–1213.